Environmental Science & Technology

pubs.acs.org/est

Article

Coupling Flow, Heat, and Reactive Transport Modeling to Reproduce *In Situ* Redox Potential Evolution: Application to an Infiltration Pond

Paula Rodríguez-Escales,* Carme Barba, Xavier Sanchez-Vila, Diederik Jacques, and Albert Folch

Cite This: *Environ. Sci. Technol.* 2020, 54, 12092−12101

Read Online

ACCESS | Metrics & More | Article Recommendations | Supporting Information

ABSTRACT: Redox potential (Eh) measurements are widely used as indicators of the dominant reduction−oxidation reactions occurring underground. Yet, Eh data are mostly used in qualitative terms, as actual values cannot be used to distinguish uniquely the dominant redox processes at a sampling point and should therefore be combined with a detailed geochemical characterization of water samples. In this work, we have intensively characterized the redox potential of the first meter of soil in an infiltration pond recharged with river water using a set of *in situ* sensors measuring every 12 min during a 1 year period. This large amount of data combined with hydrogeochemical campaigns allowed developing a reactive transport model capable of reproducing the redox potential in space and time together with the site hydrochemistry. Our results showed that redox processes were mainly driven by the amount of sedimentary organic matter in the system as well as by seasonal variation of temperature. As a subsidiary result, our work emphasizes the need to use a fully coupled model of flow, heat transport, solute transport, and the geochemical reaction network to fully reproduce the Eh observations in the topsoil.

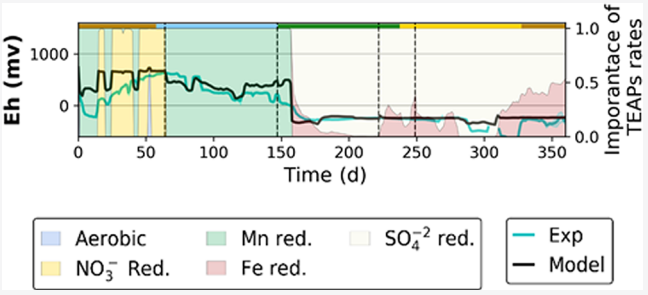

1. INTRODUCTION

The determination of the reduction−oxidation (redox) potential (Eh) in water bodies is a common practice to characterize the biogeochemistry of water samples. The redox state determines the distribution of all redox equilibria; thus, similar to pH, it can be considered as a quantity that lumps multiple processes occurring simultaneously at a corresponding sampling point in the subsurface.[1] Currently, the individual Eh measurements do not provide univocal information to characterize the dominant redox processes at a particular location. Therefore, it is only considered as a line of evidence in dominant process identification that would, otherwise, mostly rely on measuring the concentrations of redox-sensitive groundwater constituents.[2,3] There are different reasons why the redox potential cannot be used as a quantitative parameter. First is the mixed potentials due to the lack of equilibrium between the different redox couples in any water sample,[2] which hinders the determination of redox couple concentrations from the Nernst equation. Second, field Eh is typically measured with a sensor probe embedded in a flow cell from pumped water. In subsurface systems with steep redox gradients (e.g., hyporheic zones or infiltration areas), or highly heterogeneous, these measured Eh values are not representative, as point samples integrate a mixture of waters present at the capture zone of the monitoring point. Regarding Eh measurement reproducibility, a reactive transport model would require the consideration of all primary and secondary processes controlling the redox state: reduction of all aqueous- or mineral-form terminal electron acceptors (TEAPs), oxidation of electron donors (such as organic matter), solute and heat transport, and secondary geochemical processes (not necessarily involving any electron transfer) still impact reaction pathways and rates of the primary redox reactions.

Sensors capable of measuring the redox potential at a single point[4] are an alternative to flow cell sampling. Its use, which is increasing, avoids mixing interferences and can catch the redox evolution in highly dynamic systems (e.g., wetlands,[5] aquifer−stream interaction,[6] or constructed delta-lake systems[7]). Sensor data could be directly integrated into the model-based analysis of biogeochemical subsurface systems, adding significant value to field *Eh* data. Note that measuring Eh is not expensive, as it can be determined by potentiometric measurements with a non-intrusive and continuous sensor, whereas hydrogeochemical analyses are intrusive, non-continuous, and time-consuming.

Surface infiltration ponds are highly dynamic redox systems.[8−10] They are a type of managed aquifer recharge

Received: May 12, 2020
Revised: September 2, 2020
Accepted: September 8, 2020
Published: September 8, 2020

https://dx.doi.org/10.1021/acs.est.0c03056
Environ. Sci. Technol. 2020, 54, 12092−12101

(MAR) facility aimed at increasing the availability of groundwater resources by storing water in the subsurface and increasing the residence time to enhance opportunities for kinetically controlled water purification processes.[11,12] Redox reactions are driven by the simultaneous availability of TEAP-containing waters and electron donors, thus contributing to the degradation of nutrients (dissolved organic carbon,[13,14] nitrates,[8,15−17]) and organic pollutants.[18−22] Consequently, redox processes are dominant in these systems and a key aspect in the purification capacity of infiltration ponds.[20,23]

Most typically, the limiting component of a redox reaction is the concentration of the electron donor (typically, organic carbon).[24] In MAR facilities, organic matter can be supplied by the recharge water, but it can also be generated in the recharge system itself from the fixation of CO_2 by the photosynthetic organisms (algae, cyanobacteria, and plants).[25] The growth of these organisms depends on temperature, light conditions, and availability of inorganic nutrients (N and P),[26] and it is specially high during warm periods, resulting in algae blooms and surface bioclogging.[27,28] Consequently, temperature is also a key aspect controlling redox reactions.[9,29]

The spatio-temporal evolution of *Eh* is an integrated value of all the geochemical processes involved. In this way, a geochemical model capable of reproducing the Eh data should also be integrative. Although some works have focused on modeling redox processes in MAR,[9,30−34] to our knowledge, there is none integrating all the mentioned processes to understand and reproduce the spatial and temporal evolution of Eh data, mostly in the topsoil first meter where most of the redox and biological processes occur.[10,35] Note that understanding the redox temporal and spatial dynamic in an infiltration pond model will allow to understand, improve, and optimize the purification capacity of an infiltration facility, especially regarding the recalcitrant compounds like emerging organic contaminants that are degraded by co-metabolism depending on the redox reactions.[20−22]

Thus, this work is aimed at developing a reactive transport model to reproduce the Eh values measured in a real system. The model will integrate all the processes affecting the redox potential in a managed aquifer recharge facility in order to establish a method to reproduce Eh in a numerical model. The model development was constrained by 1 year data from continuous *in situ* redox potential sensors collected in an infiltration pond facility.

2. METHODOLOGY

2.1. Field Site and Monitoring Network Description. The Castellbisbal recharge facility is located in the conurbation of Barcelona (Spain). It is composed by a permanent-regime wetland (14,500 m^2) and an infiltration pond (1400 m^2). The recharge water comes from the Llobregat River. Site description, construction, and hydrogeological details are provided in section S1 in the Supporting Information.

The site was intensively monitored for 1 year (from 25/10/2016 to 24/10/2017) by continuous and non-intrusive sensors (pressure, temperature, and redox potential) located within the infiltration pond at different points and depths (Figure S1), complemented by four sampling campaigns performed during the monitoring year for geochemical analyses. Eh measurements were recorded every 12 min (a dataset of 43,800 values per sampling point) using platinum redox sensors of 1 mm thick located along stick probes (Hypnos III, MVH Consult). Measurements were taken in 10 points located at the pond surface and at different depths of ∼20 cm, ∼50 cm, ∼60 cm, and ∼70 cm (see Figure S1c). An extra sensor was placed inside a piezometer PJ, where the reference electrode (Ag/AgCl) was also installed at 6 m depth to ensure permanent wet conditions. Both depth and plain view distribution of the sensor probes and sampling points are displayed in Figure S1c. Two temperature sensors were integrated into the redox probes, one at the water pond (probe 1) and the other one at a depth of 55 cm (probe 3, Figure S1c). See the Supporting Information for more detailed information.

The four sampling campaigns were distributed along the monitored year in order to cover the seasonality as well as operational tasks affecting the infiltration rates, especially scrapping operations. The first campaign took place in winter (December 2016), the second was in spring (April 2017), the third was right after a scrapping operation following a significant (bio)clogging event detected in June 2017, and the last one was in summer (July 2017). The pond remained empty during summer holidays (August 2017). Water samples were taken at different locations: (1) infiltration pond, (2) different depths within the vadose zone (20, 50, and 90 cm), and (3) the aquifer just below the infiltration pond (PJ) (see Figure S1c). At each sampling point, some field parameters (temperature, pH, Eh, dissolved oxygen, and alkalinity) and the concentration of the main hydrogeochemical compounds (dissolved organic carbon, major cations, anions, nutrients, and metals) were obtained. The specific mineralogy of the sediments and the total iron and manganese from two random points at 30 cm depth within the infiltration pond were determined. During the sampling campaigns, we also determined the total amount of organic matter in five random points within the first 2 cm of the sediment at the infiltration pond. All the detailed information of sampling and chemical determination is available in the Supporting Information (section S2).

2.2. Reactive Transport Modeling: Processes and Governing Equations. A one-dimensional flow, heat, and reactive transport model of the infiltration pond for the Castellbisbal site was constructed using HP1[36,37] (Hydrus[38] + PHREEQC[39]). The model solves Richards' equation for flow and the convection−dispersion-reaction equation for heat and reactive transport (see section S3 of the Supporting Information for equation details and model assumptions).

Figure 1 shows all the hypothesized and key reactive processes affecting Eh in the infiltration pond and, consequently, included in the geochemical model (see also Table 1). The processes included were chosen according to the observation data and literature review. Process 1 relates to the organic matter generation (from the decomposition of algae and cyanobacteria) and its degradation to dissolved organic carbon (DOC) and ammonium (process 2). Then, DOC oxidizes using different TEAPs to inorganic carbon (process 3), which is equilibrated to different forms of carbon depending on the pH of the system and the carbonate/CO_2 equilibria. The ammonium released during organic matter mineralization and ammonium contained in the recharged water are concurrently oxidized to nitrate but solely under aerobic conditions (nitrification, process 4). Nitrate is reduced to dinitrogen gas, coupled to organic carbon oxidation (dashed line, process 3). The intermediate production of nitrite during both nitrification and denitrification was not considered, as no nitrite was measured in any sample. Note that sulfate reduction can also occur due to the re-oxidation of Fe^{+2}.[40] Goethite was

https://dx.doi.org/10.1021/acs.est.0c03056
Environ. Sci. Technol. 2020, 54, 12092−12101

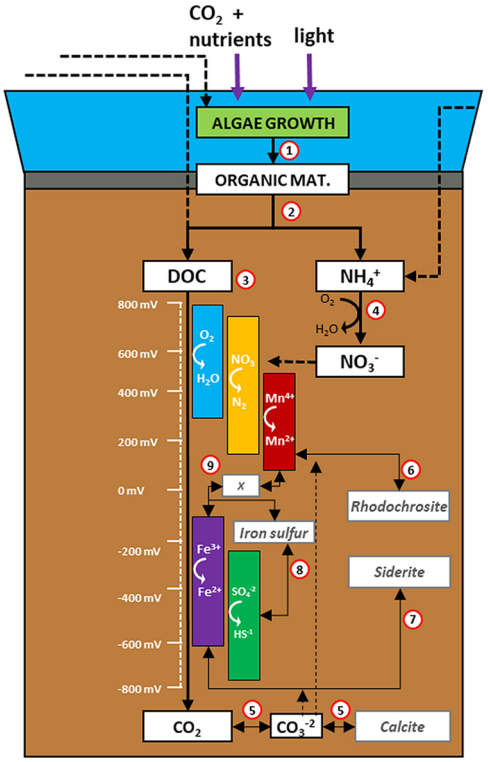

Figure 1. Biogeochemical processes considered in the reactive transport model of the Castellbisbal infiltration pond: (1) organic matter (OM) generation, (2) OM decay, (3) organic carbon oxidation with different TEAPs, (4) nitrification, (5) carbonate equilibrium and calcite precipitation, (6) rhodochrosite formation and precipitation, (7) siderite formation and precipitation, (8) iron sulfur and precipitation (in the form of mackinawite), and (9) cation exchange on soil exchange complex (X) with iron and manganese. The image shows an algae bloom generated in the infiltration pond during low flow conditions highlighting the intensive biological activity (May 2017).

selected as representative of the Fe^{+3} phase. Mineral reactions involving calcite, rhodochrosite ($MnCO_3$), siderite ($FeCO_3$), and mackinawite (FeS) (processes 5−8, respectively) as well as cation exchange of manganese and iron with soil phases (e.g., clay and organic matter; process 9) were also included in the model.

All the mentioned processes were considered as kinetically controlled (Table 1), which avoided mixed potential and irreversibility in redox processes,[41] with the exception of siderite formation (6), the exchange processes (9), and speciation reactions (such as inorganic carbon equilibrium) for which the local equilibrium assumption was implemented.

Seven cations (Na^+, K^+, NH_4^+, Ca^{+2}, Mg^{+2}, Mn^{+2}, and Fe^{+2}) were competing for one exchanger site. Equilibrium constants for cation exchange and for aqueous speciation reactions were taken from the PHREEQC database.

All processes related to DOC were temperature-dependent following the expression of O'Connell et al.[42] (see F_T, Table 1), already implemented in MAR studies.[9] Regarding the temperature effect in mineral formation, we assumed an Arrhenius dependence ($F_{T_{Ar}}$).[1,43] All the equation details and the parameter description are available in the Supporting Information (section S3).

Conceptually, Eh indicates the tendency of an environment to exchange (receive or give) electrons. Aqueous systems contain no free electrons, but the relative electron activity, as an intensity parameter, can still be defined as pe = $-\log[e^-]$. Thus, Eh is related to pe and to the concentration of the redox pairs by means of the equation $Eh = \frac{2.3RT\,pe}{F}$, where R is the gas constant, T is the temperature, and F is the Faraday's constant. In order to evaluate electron activity in quantitative terms, PHREEQC assumes, as a starting point, a redox equilibrium, which facilitated the partial equilibrium approach (PEA) to simulate redox reactions. At this point, PHREEQC incorporates a virtual electron flow between the redox pairs, calculating, automatically, pe every time step. The PEA approach has been successfully used for simulating redox processes in MAR and comparable biogeochemical subsurface systems.[9,15,16,20,41,44−46]

2.3. Model Setup and Calibration Process. To model the redox potential evolution in Castellbisbal, the site was simplified behaving as one-dimensional with the top element varying for the different periods, which incorporated the seasonal effects of clogging (decreasing in hydraulic conductivity and increasing in SOM). A decrease in hydraulic conductivity was associated to a combination of clogging processes, although they were not explicitly modeled individually: compaction, bioclogging, or gas entrapment. Thus, the developed flow, heat, and reactive transport model consisted of a vertical profile from the bottom of the infiltration pond to the groundwater (total length of 6 m), discretized into 100 equispaced nodes. The total modeled time was 1 year, covering the full period of continuous monitoring. Spatial and temporal discretizations were selected according to Péclet and Courant criteria to avoid numerical oscillations.

The model geometry involved two zones, the top one of 24 cm and the bottom one of 576 cm. The top layer was intended to reproduce the combination of clogging effects and scrapping operations described in Table 2, thus with a variation of hydraulic conductivity and sedimentary organic matter (SOM). Consequently, the model was divided into five submodels (named P-I to P-V, see Table 2) where hydraulic conductivity and SOM in the top layer changed in each one. Both parameters were manually calibrated (Table 2), although in the case of SOM, we followed the tendency observed in SOM concentration corresponding to the first 2 cm (see section S7). The hydraulic conductivity of the deeper layer remained constant in time.

Regarding the flow model boundaries, the water level of the infiltration pond was mostly specified as a Dirichlet condition for the top boundary. In August 2017, with the pond being empty from days 281−308, prescribed (null) flux was applied as an upper boundary condition (BC). Evaporation was assumed negligible. The bottom BC was specified as a constant head with the data measured in PJ (Figure S1 in the Supporting Information). For the initial conditions, we defined negative pressures in the unsaturated zone from the surface to the groundwater level, with a pressure of 0 (node 58, 3.42 cm), imposing a linear gradient of 0.359 cm/node. Porosity was fixed at 0.28, being the average of values reported in different local studies.

Afterward, a heat transport model was built. The initial temperature profile was interpolated between the top node specified at a constant temperature of 19 °C (temperature of the infiltration water at time 0) and the bottom node set at 20 °C (temperature of water in the aquifer at t = 0). Then, we applied the convection−dispersion equation (eq 5 in the

https://dx.doi.org/10.1021/acs.est.0c03056
Environ. Sci. Technol. 2020, 54, 12092−12101

Table 1. Summary of Processes, Reactions, and Rates in the Reactive Transport Model[a]

process (reaction)	kinetic rate	equilibrium constant (log K)
particulate organic matter generation from algae decomposition	$k_{gen}C_{SOM}F_T$	
degradation of particulate organic matter and dissolved organic carbon and ammonia generation	$k_{deg}C_{SOM}\left(\frac{C_{sat}+C_{DOC}}{C_{sat}}\right)F_T$	
nitrification: $2NH_4^+ + 4O_2 \rightarrow 2NO_3^- + 4H^+ + 2H_2O$	$k_{nit}\frac{C_{NH_4^+}}{C_{NH_4^+}+K_{sat,NH_4^+}}\frac{C_{NO_3^-}}{C_{NO_3^-}+K_{sat,NO_3^-}}F_T$	
oxidation of organic carbon from different TEAPs		
$CH_2O + O_2 \rightarrow HCO_3^- + H^+$		
$CH_2O + 0.8NO_3^- \rightarrow HCO_3^- + 0.4N_2 + 0.2H^+ + 0.4H_2O$		
$2CH_2O + 4MnO_2 + 6H^+ \rightarrow 2HCO_3^- + 4Mn^{+2} + 4H_2O$		
$CH_2O + 4FeO(OH) + 7H^+ \rightarrow HCO_3^- + 4Fe^{+2} + 6H_2O$	$C_{DOC}\sum_{i=1}^{n}\left(k_i\frac{C_{EA}}{C_{EA}+K_{sat,EA}}\prod_{j=1}^{m}\frac{C_{j,EA}+K_{inh,j,AE}}{K_{inh,j,EA}}\right)F_T$	
$2CH_2O + SO_4^{-2} \rightarrow HCO_3^- + HS^- + H^+$		
secondary mineral reactions		
calcite precipitation: $CaCO_3 \leftrightarrow Ca^{+2} + CO_3^{-2}$	$k_{Cc}\left(\frac{m_{Cc}}{m_{0,Cc}}\right)^{0.6}p(1-\Omega_{Cc})^{0.6}$	
rhodochrosite precipitation: $MnCO_3 \leftrightarrow Mn^{+2} + CO_3^{-2}$	$k_{Rhod}(1-\Omega_{Rhod})F_{T_{Ar}}$	
iron sulfur precipitation: $FeS \leftrightarrow Fe^{+2} + S^{-2}$	$k_{Mack}(1-\Omega_{Mack})F_{T_{Ar}}$	
siderite: $FeCO_3 \leftrightarrow Fe^{+2} + CO_3^{-2}$		−10.89
cation exchange reactions: $Cat^{+i} + iX^- \leftrightarrow CatX_i$; Cat{$Na^+$, K^+, NH_4^+, Ca^{+2}, Mg^{+2}, Mn^{+2}, Fe^{+2}}		various

[a]An extended version of this table with all the stoichiometric relationships and parameter description can be found in the Supporting Information.

Table 2. Periods Considered in the Model and Fitted Values of Hydraulic Conductivity and SOM Concentration of the Top Layer

				surface layer	
sub-models	starting date	duration (final day)	characteristics	K (cm/d)	sedimentary organic matter (M)[a]
P-I	24/10/16	64	initial conditions	25	0.25
P-II	27/12/16	83 (147)	intermediate infiltration rate period ended with a heavy rainfall event	15	0.41
P-III	20/03/17	75 (222)	low infiltration rate physical and biological clogging	5	1.15
P-IV	03/06/17	27 (249)	period after scrapping high infiltration rate	600	0.08
P-V	30/06/17	116 (365)	fluctuation of infiltration rate flow discontinued in the middle of the period (01-31/08/2017)	30	0.25

[a]SOM concentrations were converted to mol/L considering a porosity of 0.28 and a soil density of 1.7 kg/L.

Supporting Information) to solve the heat transport. Temperatures of the infiltration water and at the aquifer (PJ) were prescribed daily as upper and lower boundary conditions, respectively. The thermal parameters of the soil were set to default values provided by Chung and Horton[47] for a sandy material. The heat transport model was evaluated by comparing the temperature calculated at a depth of 55 cm with the data provided by the temperature sensor at this depth (probe 3, Figure S1).

Last, a reactive transport model was constructed. The geochemical signature of the initial and the inflow solutions are presented in section S4 of the Supporting Information. The reactive transport model was calibrated manually, trying to get the best fit to the oxidation−reduction potential measured at the probes with respect to the Eh values provided by the HP1 model as well as to DOC, TEAPs, ammonium, and pH recorded from the four hydrogeochemical campaigns. Calibration was focused on the first meter of the model domain since this was the zone intensively monitored. To facilitate calibration, we set all the saturation constants as well as the inhibition parameters from the geochemical model fixed.

3. RESULTS AND DISCUSSION

3.1. Model Capable of Reproducing the Eh Field Measurements. The first step in the modeling effort was the coupled flow and heat transport model. Figure 2 shows that the model captured the main trends of the evolution of the infiltration with time by manually calibrating the saturated hydraulic conductivity (K_s) in the top layer ranging from 5 to 600 cm/d (Table 2). The lowest value was set at spring and summer (P-III), in agreement with the lowest infiltration rate due to clogging (flooding of the site during a rain event and non-scrapping for 6 months) and the algae bloom observed in the infiltration pond. A K_s value of 600 cm/d was assigned to the top layer after scrapping (P-IV), equal to that for the bottom layer (not affected by clogging in our model).

https://dx.doi.org/10.1021/acs.est.0c03056
Environ. Sci. Technol. 2020, 54, 12092−12101

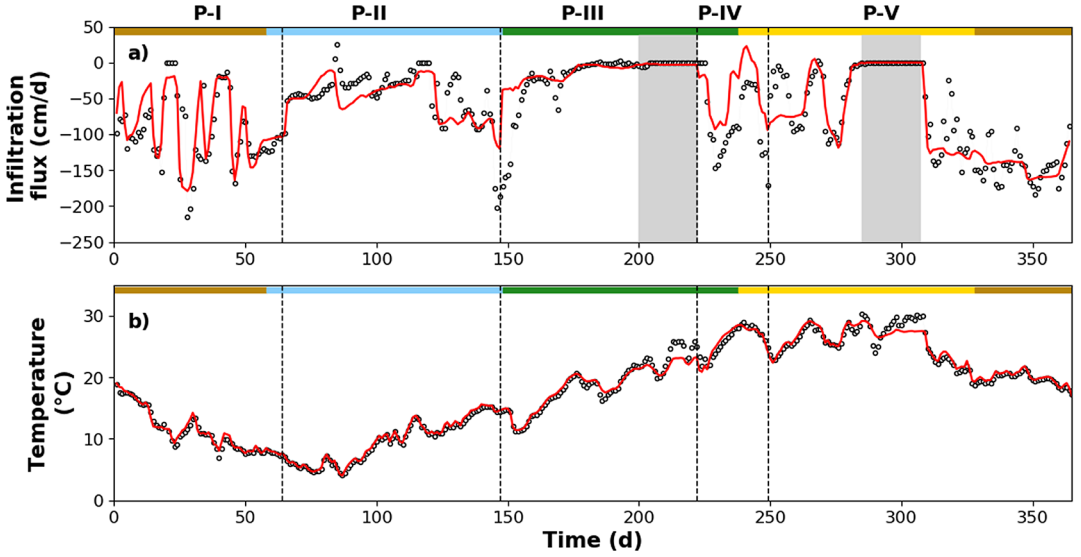

Figure 2. (a) Evolution of the infiltrating flow rate. (b) Temperature evolution at 55 cm depth during the five modeled periods. The red lines are the result of the coupled flow and heat transport model, and the black points are the experimental data. The season evolution is presented on the top bar using a color code: brown for fall, blue for winter, green for spring, and yellow for summer. The gray zones represent periods when recharge was discontinued: the first one is for scrapping actions, and in the second one, the pond was dry.

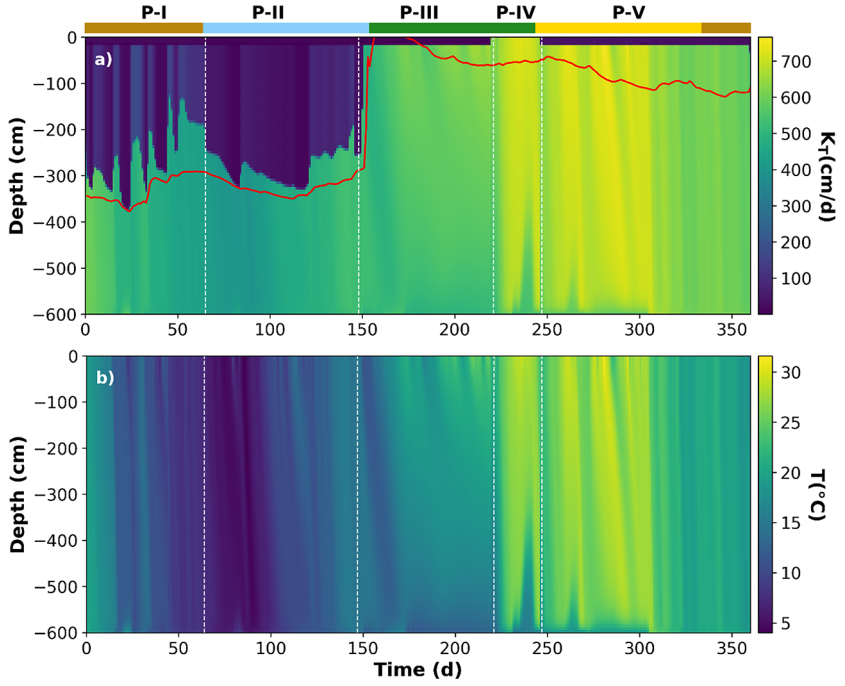

Figure 3. Variation of (a) effective hydraulic conductivity and (b) temperature with depth as a function of time. The season evolution is presented on the top bar, similar to Figure 2. The red line in panel (a) reflects the groundwater level evolution measured in PJ.

Nevertheless, this value decreased to 30 cm/d in less than 1 month (P-V), indicating that summer scrapping did not guarantee significant infiltration capacity for long.

Regarding the heat transport model, the model fitting for temperature is quite good at a depth of 55 cm (Figure 2b). Figure 3a shows the hydraulic conductivity (K_T) as a function of space and time, affected by density and viscosity dependence on T (eq7 of the Supporting Information) and by soil water content (Figure S2). The actual range of K_T values is quite large [1.42×10^{-2} to 766] cm/d, with the lowest values taking place in winter, affected by the low water content values, and the highest ones corresponding to fully saturated conditions in spring/summer, mainly affected by changes in viscosity and density.

The next step was building the full reactive transport model. Calibration was performed on a number of transport and reaction model parameters (Table S3, Supporting Information) as well as the initial amount of SOM in the surface layer corresponding to each model period (Table 2). Estimated SOM values correlated inversely with K, indicating that the former are also affected by seasonality, or in other words, that biomass growth played an important role in the source of SOM, being the electron donor in the system. Notice that the SOM-calibrated values were much lower than the experimental

https://dx.doi.org/10.1021/acs.est.0c03056
Environ. Sci. Technol. 2020, 54, 12092−12101

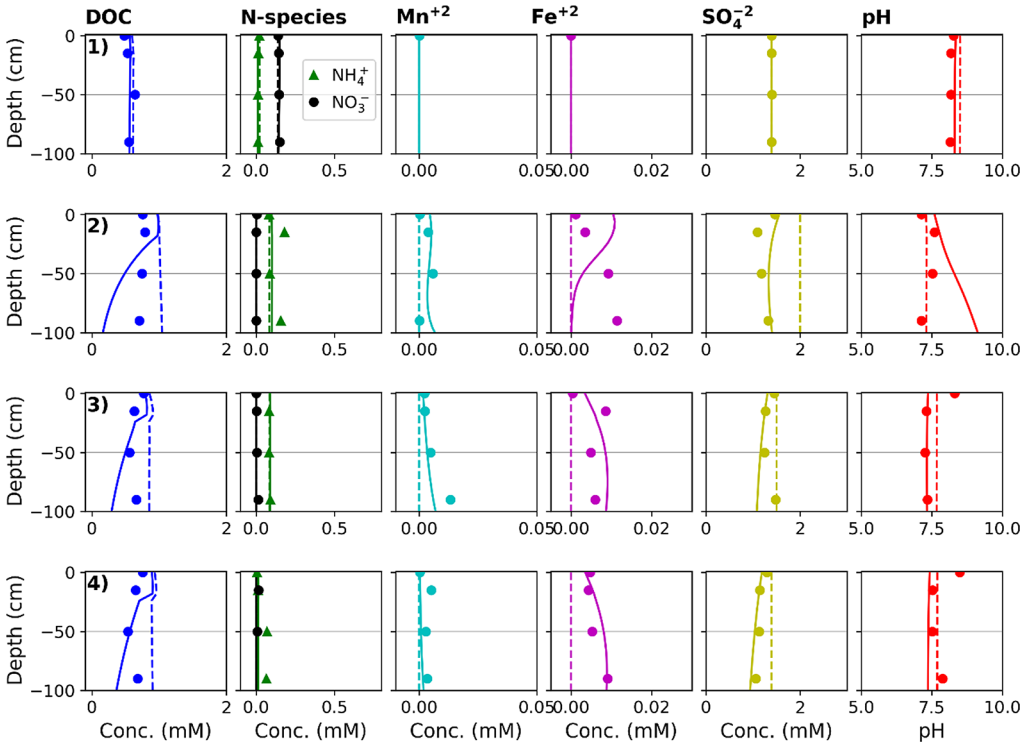

Figure 4. Evolution of DOC, ammonium, and TEAPs in the four sampling campaigns. Points indicate the experimental data, and solid lines are values supplied by the model. Dashed lines are the result model without considering DOC degradation. Each row corresponds to one sampling campaign: from top to bottom: December 2016, April 2017, June 2017, and July 2017.

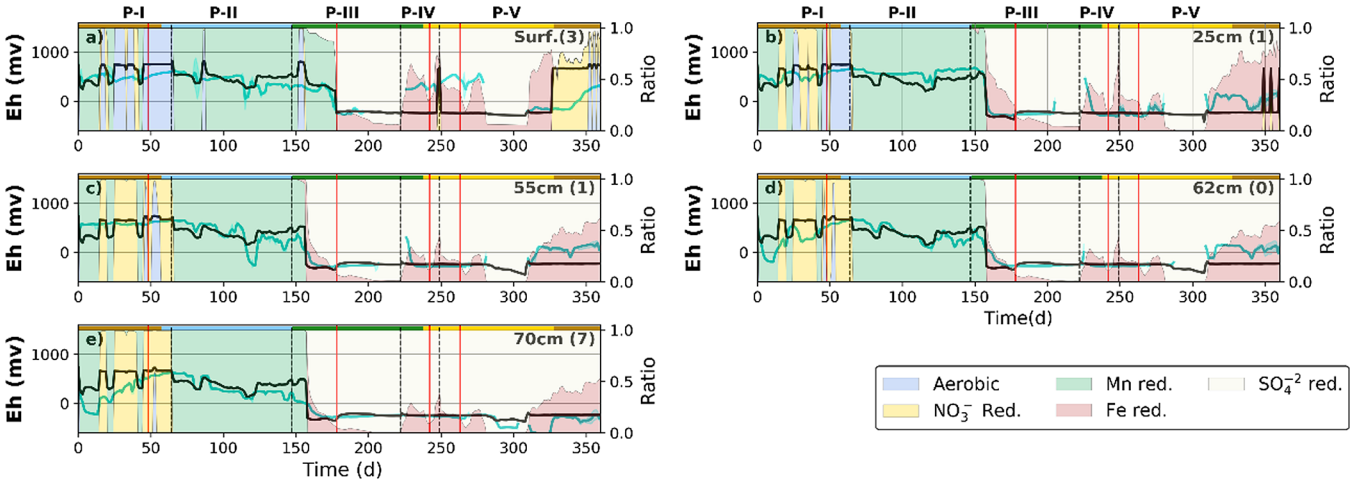

Figure 5. Evolution in time of redox potential at different depths (from the surface to 70 cm depth). The blue line represents the daily arithmetic average value of redox potential (from measurements taken every 12 min), presented as an area bounded by the plus/minus one standard deviation (hardly visible in most points). The redox potential information during dry periods is not shown since the redox sensor probe had high erratic oscillations due to low connectivity. The black line represents the model results. The red vertical lines represent the sampling dates for hydrochemistry. The background color of the plot reflects the relative importance of the different reaction rates in the total degradation of DOC. This importance (ratio) was calculated by dividing each rate by the sum of the total rates involved in TEAP reduction.

ones (Figure S3), which is partially explained by the fact that the former were representative of the model top layer (24 cm) while the latter only referred to the top 2 cm. Nevertheless, they followed the same trend.

The geochemical model, fitted by considering both hydrochemistry and Eh data, captured the main evolution of redox-related compounds and pH (Figure 4). In December, the system operated under aerobic conditions, with ammonium oxidizing to nitrate. The other TEAPs (nitrate, manganese, iron, and sulfate) remained stable, indicating the poor activity of the system, probably because of low temperatures; indeed, the results are quite similar without organic matter degradation (dashed lines, Figure 4). In the subsequent three campaigns, all the TEAPs were activated and the system achieved reducing conditions: nitrate and sulfate were completely depleted, and Mn(II) and Fe(II) were produced. These observations were coherent with the dominating rates for the different periods (Figure 5 and Figure S4), where Mn reduction dominated in winter and early spring and iron and sulfate reductions were the driving processes during spring and summer. Iron and

https://dx.doi.org/10.1021/acs.est.0c03056
Environ. Sci. Technol. 2020, 54, 12092−12101

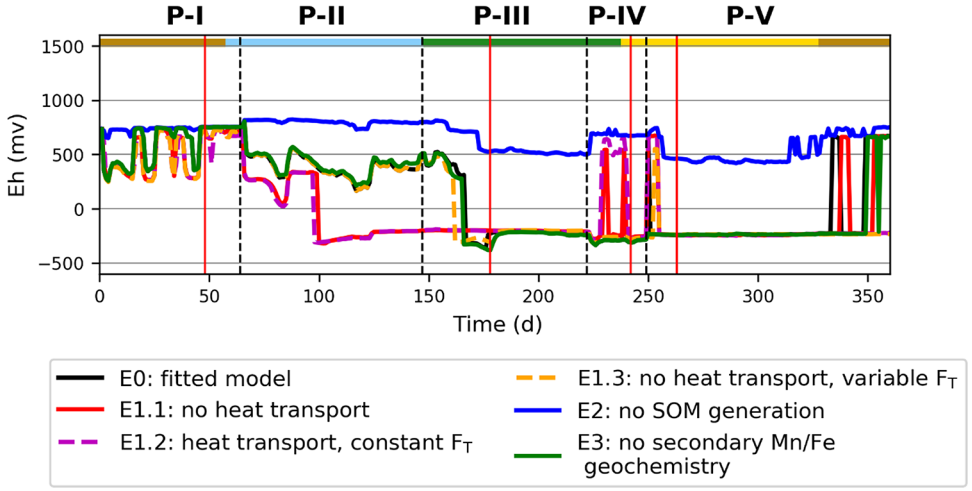

Figure 6. Sensitivity of the model response for Eh evolution as a function of time at the surface of the infiltration pond when including some alternative models neglecting one or more processes.

sulfate reduction coexistence was associated to the sulfate reduction due to the re-oxidation of Fe(II).[40] The activation of more reducing processes was clearly related with increasing SOM concentration during the warm periods of the year, in line with the observations in infiltration ponds elsewhere.[48,49]

The Mn^{2+} and Fe^{2+} profiles were achieved by incorporating secondary processes into the model: precipitation of rhodochrosite and mackinawite, respectively, and cation exchange. These assumptions were based on previous work where the authors observed these minerals forming in batch redox experiments with similar sediments and groundwater.[50] Mackinawite precipitation was also identified in field campaigns (as a black sediment), and its formation has been described in similar works.[50−53] Although the model fitted the general tendency, in the April campaign, iron and pH fittings were not well adjusted, which we explain by heterogeneity in the system delaying the iron reducing front. On the other hand, despite several modeled scenarios showing that mackinawite precipitation was the most significant process governing Fe(II), we did not neglect the impact of exchange processes with SOM (as the clay content in the soil was negligible) on iron dynamics.

Figure 5 shows the temporal evolution of the redox potential (mean plus/minus one standard deviation of the 120 daily measurements), together with the model results at different depths. The model fitted quite well the general tendency of the redox potential, showing the highest aerobic potentials (positive Eh values, also extending along the vertical) during the colder periods. This seasonality was associated to the amount of SOM as well as the increasing geochemical reaction rates in the warmer periods. During the first weeks of P-I, we observed some model discrepancies that were attributed to the stabilization of Eh sensors. Also note that Eh measurements were not compensated with pH since we did not have the same spatial/temporal resolution in the latter; moreover, pH variation ranged only about 1 unit. In general terms, the fittings were better for the deeper sensors (55, 62, and 70 cm), probably because deep fluxes are more homogeneous than those near the surface. The model fitting indicates that the computation of pe performed by the PEA in PHREEQC properly represents the Eh values measured by several sensors.

3.2. Evaluating the Influence of Different Processes upon the Redox Potential. In this section, we tested the significance of some processes in the resulting geochemical model, emphasizing their impact upon the Eh data (Figure 6). For that, we ran different scenarios, always compared to the model presented in the previous section (termed E0). In the first alternative scenario (E1), we tested the effect of temperature. It was divided in three sub-scenarios: E1.1 is where we neglected the impact of heat transport in flow and geochemical processes; here, temperature was fixed at the average value of the whole domain (18 °C) for all times and depths. E1.2 is where heat transport was considered but neglected in the reaction rates (constant F_T, assuming 18 °C), and E1.3 is where heat transport was also neglected but F_T was recalculated from the seasonal constant temperature introduced in each period. In scenario E2, we neglected the role of SOM generation due to the photosynthetic organisms; numerically, this implied setting the initial amount of SOM to 0 in all five periods considered (recall Table 2). Finally, in scenario E3, we neglected all the secondary processes associated to reduced iron and manganese geochemistry.

From these scenarios, the amount of organic matter (E2) is the most significant variable for simulating the redox potential dynamics since it is the main electron donor driving the redox reactions. The fixation of CO_2 and the subsequent formation of DOC are the main source of electrons, well above the DOC supplied by the recharge water. Also, considering the effect of temperature in reaction rates (F_T) is relevant (E1.3), even if a full heat transport model is not implemented. Indeed, the impact of heat transport in water velocity did not modify significantly the modeled Eh (E1.1 and E1.2). Finally, note that E3 is quite similar to the reference scenario; we attribute it to secondary geochemical processes (precipitation and cation exchange) only affecting the fate of Mn^{+2}/Fe^{+2} but not Eh since these two components are already in reduced conditions.

3.3. Implications for Reduction−Oxidation Potential Monitoring in Environmental Systems. In this work, we have shown that the reduction−oxidation potential measured under natural conditions with continuous and *in situ* sensor probes can be reproduced by a geochemical model. This fact exhibits and confirms that the traditional Eh sampling methodology is not adequate to be incorporated into a mathematical model since it is not valid and not representative of individual points; consequently, these measurements have hardly any possibility to be reproduced. In our case, in all

https://dx.doi.org/10.1021/acs.est.0c03056
Environ. Sci. Technol. 2020, 54, 12092−12101

sampling points, except the surface water, we observed a bias in Eh measurements (see section S9 and Figure S5). In winter, traditional sampling led to more reducing values compared with *in situ* measurements, whereas in spring/summer periods, more aerobic values were measured. Thus, the use of Eh non-invasive point sensors at different depths is quite recommendable, especially if a numerical reproduction of the site is required. We still recommend combining this information with traditional hydrogeochemical sampling campaigns performed at different seasons, monitoring, at least, the TEAPs and the organic matter dynamics.

Our results also demonstrated that acknowledging the effects of temperature in reaction rates is crucial to reproduce Eh trends in space and time; thus, infiltration pond models should always account for the temperature factor (F_T) in geochemical rates. Consequently, it is highly recommendable to install temperature sensors at different depths of the experimental sites in order to catch the seasonal evolution of temperature. These recommendations are extended to similar models developed, e.g,. in constructed wetlands or the hyporheic zone.

We found that the seasonal activity of photosynthetic organisms is a relevant factor affecting both physical infiltration processes (via bioclogging) and the geochemical redox processes (being a source of organic carbon and thus becoming a prime process in the vertical distribution of redox potential).

Understanding the redox processes in an infiltration system is quite important to assess the real purification capacity of a recharge facility, in particular, regarding emerging organic compounds. In this way, this work is a step forward the redox characterization and process quantification, which will allow to improve the understanding of the fate of these compounds.

■ ASSOCIATED CONTENT

Supporting Information

The Supporting Information is available free of charge at https://pubs.acs.org/doi/10.1021/acs.est.0c03056.

> Detailed site description; field site monitoring; model construction; tables of initial/boundary concentrations and fitted parameters of the reactive transport; and figures about the evolution of water content, evolution of sedimentary organic matter, TEAP rate's plume, and comparison of different experimental Eh values (PDF)

■ AUTHOR INFORMATION

Corresponding Author

Paula Rodríguez-Escales − *Department of Civil and Environmental Engineering, Universitat Politècnica de Catalunya, 08034 Barcelona, Spain; Associated Unit: Hydrogeology Group (UPC-CSIC), 08034 Barcelona, Spain;* orcid.org/0000-0003-1011-5306; Email: paula.rodriguez.escales@upc.edu

Authors

Carme Barba − *Department of Civil and Environmental Engineering, Universitat Politècnica de Catalunya, 08034 Barcelona, Spain; Associated Unit: Hydrogeology Group (UPC-CSIC), 08034 Barcelona, Spain*

Xavier Sanchez-Vila − *Department of Civil and Environmental Engineering, Universitat Politècnica de Catalunya, 08034 Barcelona, Spain; Associated Unit: Hydrogeology Group (UPC-CSIC), 08034 Barcelona, Spain*

Diederik Jacques − *Engineered and Geosystems Analysis, Institute for Environment, Mol 2400, Belgium*

Albert Folch − *Department of Civil and Environmental Engineering, Universitat Politècnica de Catalunya, 08034 Barcelona, Spain; Associated Unit: Hydrogeology Group (UPC-CSIC), 08034 Barcelona, Spain*

Complete contact information is available at: https://pubs.acs.org/10.1021/acs.est.0c03056

Notes

The authors declare no competing financial interest.
‖Serra Hunter Fellow (A.F.)

■ ACKNOWLEDGMENTS

This work was financially supported by MONOPOLIOS (RTI2018-101990-B-100, MINECO/FEDER), the EU project MARADENTRO (PCI2019-103425-WW2017), the Catalan Research Project RESTORA (ACA210/18/00040), and AGAUR (AQU - 2017 SGR 1485). The authors wish to acknowledge Comunitat d'Usuaris d'Aigües de la Cubeta de Sant Andreu de la Barca (CUACSA) and the Agència Catalana de l'Aigua for their cooperation.

■ REFERENCES

(1) Appelo, C. A. J.; Postma, D. *Geochemistry, groundwater and pollution*; CRC Press: 2004.

(2) Lindberg, R. D.; Runnells, D. D. Ground Water Redox Reactions: An Analysis of Equilibrium State Applied to Eh Measurements and Geochemical Modeling. *Science* **1984**, *225*, 925.

(3) Christensen, T. H.; Bjerg, P. L.; Banwart, S. A.; Jakobsen, R.; Heron, G.; Albrechtsen, H.-J. Characterization of redox conditions in groundwater contaminant plumes. *J. Contam. Hydrol.* **2000**, *45*, 165−241.

(4) Vorenhout, M.; van der Geest, H. G.; van Marum, D.; Wattel, K.; Eijsackers, H. J. P. Automated and continuous redox potential measurements in soil. *J. Environ. Qual.* **2004**, *33*, 1562−1567.

(5) Lee, P. O.; Shoemaker, C.; Olson, J. B. Wetland Soil Properties and Resident Bacterial Communities Are Influenced by Changes in Elevation. *Wetlands* **2019**, *39*, 99−112.

(6) Wallace, C. D.; Sawyer, A. H.; Barnes, R. T. Spectral analysis of continuous redox data reveals geochemical dynamics near the stream−aquifer interface. *Hydrol. Processes* **2019**, *33*, 405−413.

(7) Vonk, J. A.; Rombouts, T.; Schoorl, J. C.; Serne, P.; Westerveld, J. W.; Cornelissen, P.; van der Geest, H. G. Impact of water drawdown and rewetting on sediment nutrient-dynamics in a constructed delta-lake system (Oostvaardersplassen, The Netherlands): A mesocosm study. *Ecol. Eng.* **2017**, *108*, 396−405.

(8) Barba, C.; Folch, A.; Gaju, N.; Sanchez-Vila, X.; Carrasquilla, M.; Grau-Martínez, A.; Martínez-Alonso, M. Microbial community changes induced by Managed Aquifer Recharge activities: linking hydrogeological and biological processes. *Hydrol. Earth Syst. Sci.* **2019**, *23*, 139−154.

(9) Greskowiak, J.; Prommer, H.; Massmann, G.; Nützmann, G. Modeling Seasonal Redox Dynamics and the Corresponding Fate of the Pharmaceutical Residue Phenazone During Artificial Recharge of Groundwater. *Environ. Sci. Technol.* **2006**, *40*, 6615−6621.

(10) Massmann, G.; Pekdeger, A.; Merz, C. Redox processes in the Oderbruch polder groundwater flow system in Germany. *Appl Geochemistry* **2004**, *19*, 863−886.

(11) Dillon, P.; Stuyfzand, P.; Grischek, T.; Lluria, M.; Pyne, R. D. G.; Jain, R. C.; Bear, J.; Schwarz, J.; Wang, W.; Fernandez, E.; Stefan, C.; Pettenati, M.; van der Gun, J.; Sprenger, C.; Massmann, G.; Scanlon, B. R.; Xanke, J.; Jokela, P.; Zheng, Y.; Rossetto, R.; Shamrukh, M.; Pavelic, P.; Murray, E.; Ross, A.; Bonilla Valverde, J. P.; Palma Nava, A.; Ansems, N.; Posavec, K.; Ha, K.; Martin, R.;

Sapiano, M. Sixty years of global progress in managed aquifer recharge. *Hydrogeol. J.* **2018**, *27*, 1−30.
(12) Rodríguez-Escales, P.; Canelles, A.; Sanchez-Vila, X.; Folch, A.; Kurtzman, D.; Rossetto, R.; Fernández-Escalante, E.; Lobo-Ferreira, J. P.; Sapiano, M.; San-Sebastián, J.; Schüth, C. A risk assessment methodology to evaluate the risk failure of managed aquifer recharge in the Mediterranean Basin. *Hydrol. Earth Syst. Sci.* **2018**, *22*, 3213−3227.
(13) Li, D.; Sharp, J. O.; Saikaly, P. E.; Ali, S.; Alidina, M.; Alarawi, M. S.; Keller, S.; Hoppe-Jones, C.; Drewes, J. E. Dissolved Organic Carbon Influences Microbial Community Composition and Diversity in Managed Aquifer Recharge Systems. *Appl. Environ. Microbiol.* **2012**, *78*, 6819.
(14) Rolle, M.; Clement, T. P.; Sethi, R.; Di Molfetta, A. A kinetic approach for simulating redox-controlled fringe and core biodegradation processes in groundwater: model development and application to a landfill site in Piedmont, Italy. *Hydrol. Processes* **2008**, *22*, 4905−4921.
(15) Rodríguez-Escales, P.; Folch, A.; van Breukelen, B. M.; Vidal-Gavilan, G.; Sanchez-Vila, X. Modeling long term Enhanced in situ Biodenitrification and induced heterogeneity in column experiments under different feeding strategies. *J. Hydrol.* **2016**, *538*, 127−137.
(16) Rodríguez-Escales, P.; Folch, A.; Vidal-Gavilan, G.; van Breukelen, B. M. Modeling biogeochemical processes and isotope fractionation of enhanced in situ biodenitrification in a fractured aquifer. *Chem. Geol.* **2016**, *425*, 52−64.
(17) Barba, C.; Folch, A.; Sanchez-Vila, X.; Martínez-Alonso, M.; Gaju, N. Are dominant microbial sub-surface communities affected by water quality and soil characteristics? *J. Environ. Manage.* **2019**, *237*, 332−343.
(18) van Breukelen, B. M.; Griffioen, J.; Röling, W. F. M.; van Verseveld, H. W. Reactive transport modelling of biogeochemical processes and carbon isotope geochemistry inside a landfill leachate plume. *J. Contam. Hydrol.* **2004**, *70*, 249−269.
(19) Greskowiak, J.; Hamann, E.; Burke, V.; Massmann, G. The uncertainty of biodegradation rate constants of emerging organic compounds in soil and groundwater − A compilation of literature values for 82 substances. *Water Res.* **2017**, *126*, 122−133.
(20) Rodríguez-Escales, P.; Fernàndez-Garcia, D.; Drechsel, J.; Folch, A.; Sanchez-Vila, X. Improving degradation of emerging organic compounds by applying chaotic advection in Managed Aquifer Recharge in randomly heterogeneous porous media. *Water Resour. Res.* **2017**, *53*, 4376−4392.
(21) Rodríguez-Escales, P.; Sanchez-Vila, X. Modeling the fate of UV filters in subsurface: Co-metabolic degradation and the role of biomass in sorption processes. *Water Res.* **2020**, *168*, 115192.
(22) Rodríguez-Escales, P.; Sanchez-Vila, X. Fate of sulfamethoxazole in groundwater: Conceptualizing and modeling metabolite formation under different redox conditions. *Water Res.* **2016**, *105*, 540−550.
(23) Freixa, A.; Rubol, S.; Carles-Brangarí, A.; Fernàndez-Garcia, D.; Butturini, A.; Sanchez-Vila, X.; Romaní, A. M. The effects of sediment depth and oxygen concentration on the use of organic matter: An experimental study using an infiltration sediment tank. *Sci. Total Environ.* **2016**, *540*, 20−31.
(24) Rivett, M. O.; Buss, S. R.; Morgan, P.; Smith, J. W. N.; Bemment, C. D. Nitrate attenuation in groundwater: A review of biogeochemical controlling processes. *Water Res.* **2008**, *42*, 4215−4232.
(25) Panno, S. V.; Kelly, W. R.; Hackley, K. C.; Hwang, H.-H.; Martinsek, A. T. Sources and fate of nitrate in the Illinois River Basin, Illinois. *J. Hydrol.* **2008**, *359*, 174−188.
(26) Dou, M.; Ma, X.; Zhang, Y.; Zhang, Y.; Shi, Y. Modeling the interaction of light and nutrients as factors driving lake eutrophication. *Ecol. Modell.* **2019**, *400*, 41−52.
(27) Dutta, T.; Carles-Brangarí, A.; Fernàndez-Garcia, D.; Rubol, S.; Tirado-Conde, J.; Sanchez-Vila, X. Vadose zone oxygen (O_2) dynamics during drying and wetting cycles: An artificial recharge laboratory experiment. *J. Hydrol.* **2015**, *527*, 151−159.
(28) Pedretti, D.; Barahona-Palomo, M.; Bolster, D.; Sanchez-Vila, X.; Fernàndez-Garcia, D. A quick and inexpensive method to quantify spatially variable infiltration capacity for artificial recharge ponds using photographic images. *J. Hydrol.* **2012**, *430*−*431*, 118−126.
(29) Massmann, G.; Greskowiak, J.; Dünnbier, U.; Zuehlke, S.; Knappe, A.; Pekdeger, A. The impact of variable temperatures on the redox conditions and the behaviour of pharmaceutical residues during artificial recharge. *J. Hydrol.* **2006**, *328*, 141−156.
(30) Henzler, A. F.; Greskowiak, J.; Massmann, G. Seasonality of temperatures and redox zonations during bank filtration − A modeling approach. *J. Hydrol.* **2016**, *535*, 282−292.
(31) Greskowiak, J.; Prommer, H.; Vanderzalm, J.; Pavelic, P.; Dillon, P. Modeling of carbon cycling and biogeochemical changes during injection and recovery of reclaimed water at Bolivar, South Australia. *Water Resour. Res.* **2005**, *41*, W10418.
(32) Prommer, H.; Stuyfzand, P. J. Identification of Temperature-Dependent Water Quality Changes during a Deep Well Injection Experiment in a Pyritic Aquifer. *Environ. Sci. Technol.* **2005**, *39*, 2200−2209.
(33) Seibert, S.; Atteia, O.; Ursula Salmon, S.; Siade, A.; Douglas, G.; Prommer, H. Identification and quantification of redox and pH buffering processes in a heterogeneous, low carbonate aquifer during managed aquifer recharge. *Water Resour. Res.* **2016**, *52*, 4003−4025.
(34) Schafer, D.; Sun, J.; Jamieson, J.; Siade, A. J.; Atteia, O.; Prommer, H. Model-Based Analysis of Reactive Transport Processes Governing Fluoride and Phosphate Release and Attenuation during Managed Aquifer Recharge. *Environ. Sci. Technol.* **2020**, *54*, 2800−2811.
(35) Greskowiak, J.; Prommer, H.; Massmann, G.; Johnston, C. D.; Nützmann, G.; Pekdeger, A. The impact of variably saturated conditions on hydrogeochemical changes during artificial recharge of groundwater. *Appl. Geochem.* **2005**, *20*, 1409−1426.
(36) Jacques, D.; Šimůnek, J.; Mallants, D.; Van Genuchten, M. T. The HPx software for multicomponent reactive transport during variably-saturated flow: Recent developments and applications. *J. Hydrol. Hydromech.* **2018**, *66*, 211−226.
(37) Jacques, D.; Šimůnek, J.; Mallants, D.; van Genuchten, M. T. Modeling Coupled Hydrologic and Chemical Processes: Long-Term Uranium Transport following Phosphorus Fertilization. *Vadose Zone J.* **2008**, *7*, 698−711.
(38) Šimůnek, J.; van Genuchten, M. T.; Šejna, M. HYDRUS: Model use, calibration and validation. *Trans. ASABE* **2012**, *55*, 13.
(39) Parkhurst, D. L.; Appelo, C. A. J. *User's guide to PHREEQC (version 2) - a computer program for speciation, reaction-path, 1D-transport, and inverse geochemical calculations*; U.S. GEOLOGICAL SURVEY: 1999.
(40) Postma, D.; Jakobsen, R. Redox zonation: Equilibrium constraints on the Fe(III)/SO_4-reduction interface. *Geochim. Cosmochim. Acta* **1996**, *60*, 3169−3175.
(41) Brun, A.; Engesgaard, P. Modelling of transport and biogeochemical processes in pollution plumes: literature review and model development. *J. Hydrol.* **2002**, *256*, 211−227.
(42) O'Connell, A. M. Microbial decomposition (respiration) of litter in eucalypt forests of South-Western Australia: An empirical model based on laboratory incubations. *Soil Biol. Biochem.* **1990**, *22*, 153−160.
(43) Palandri, J. L.; Kharaka, Y. K. *A compilation of rate parameters of water-mineral interaction kinetics interaction for application to geochemical modeling*; U.S. GEOLOGICAL SURVEY: 2004.
(44) Prommer, H.; Tuxen, N.; Bjerg, P. L. Fringe-controlled natural attenuation of phenoxy acids in a landfill plume: integration of field-scale processes by reactive transport modeling. *Environ. Sci. Technol.* **2006**, *40*, 4732−4738.
(45) Prommer, H.; Grassi, M. E.; Davis, A. C.; Patterson, B. M. Modeling of Microbial Dynamics and Geochemical Changes in a Metal Bioprecipitation Experiment. *Environ. Sci. Technol.* **2007**, *41*, 8433−8438.
(46) Jakobsen, R.; Postma, D. Redox zoning, rates of sulfate reduction and interactions with Fe-reduction and methanogenesis in a

https://dx.doi.org/10.1021/acs.est.0c03056
Environ. Sci. Technol. 2020, 54, 12092−12101

shallow sandy aquifer, Rømø, Denmark. *Geochim. Cosmochim. Acta* **1999**, *63*, 137−151.
(47) Chung, S.-O.; Horton, R. Soil heat and water flow with a partial surface mulch. *Water Resour. Res.* **1987**, *23*, 2175−2186.
(48) Grau-Martínez, A.; Folch, A.; Torrentó, C.; Valhondo, C.; Barba, C.; Domènech, C.; Soler, A.; Otero, N. Monitoring induced denitrification during managed aquifer recharge in an infiltration pond. *J. Hydrol.* **2018**, *561*, 123−135.
(49) Barba, C. *Physical, geochemical and microbial parameters driving the improvement of water quality in Managed Aquifer Recharge*; Universitat Politècnica de Catalunya: Barcelona, 2018.
(50) Barbieri, M.; Carrera, J.; Sanchez-Vila, X.; Ayora, C.; Cama, J.; Köck-Schulmeyer, M.; López de Alda, M.; Barceló, D.; Tobella Brunet, J.; Hernández García, M. Microcosm experiments to control anaerobic redox conditions when studying the fate of organic micropollutants in aquifer material. *J. Contam. Hydrol.* **2011**, *126*, 330−345.
(51) Rickard, D.; Luther, G. W. Chemistry of Iron Sulfides. *Chem. Rev.* **2007**, *107*, 514−562.
(52) Williams, K. H.; Kemna, A.; Wilkins, M. J.; Druhan, J.; Arntzen, E.; N'Guessan, A. L.; Long, P. E.; Hubbard, S. S.; Banfield, J. F. Geophysical Monitoring of Coupled Microbial and Geochemical Processes During Stimulated Subsurface Bioremediation. *Environ. Sci. Technol.* **2009**, *43*, 6717−6723.
(53) Van Cappellen, P.; Wang, Y. Cycling of iron and manganese in surface sediments; a general theory for the coupled transport and reaction of carbon, oxygen, nitrogen, sulfur, iron, and manganese. *Am. J. Sci.* **1996**, *296*, 197−243.

https://dx.doi.org/10.1021/acs.est.0c03056
Environ. Sci. Technol. 2020, 54, 12092−12101